

Atomic-number dependence of soft-x-ray emission from various targets irradiated by a 0.53- μm -wavelength laser

T. Mochizuki, T. Yabe, K. Okada, M. Hamada, N. Ikeda, S. Kiyokawa, and C. Yamanaka

Institute of Laser Engineering, Osaka University, 2-6 Yamada-oka, Suita, Osaka 565, Japan

(Received 4 September 1984; revised manuscript received 6 August 1985)

The spectrum-resolved radiant energies in the 0.1–1.6 keV range from various plane targets irradiated by a 0.53- μm laser at 0.1–1.0-nsec pulses with intensities of 10^{13} – 2×10^{15} W/cm² are obtained. The conversion efficiency increases with the laser-pulse duration. The physical meaning of the obtained spectrum, such as the correspondence between the emitted photons and the responsible plasma density and temperature region, is clarified from the computational studies by using the one-dimensional hydrodynamic Lagrangian code which is coupled with a nonlocal thermodynamic equilibrium average ion model and multigroup radiation transport. The energy transport of the absorbed laser energy is discussed. Atomic-number dependences of the obtained spectrum and x-ray conversion efficiency show an undulatory structure. This is well reproduced qualitatively and to some extent quantitatively by the code calculation and the contributions of the electronic transitions in different orbital shells are approximately estimated.

I. INTRODUCTION

Experimental investigation of x-ray generation in laser-produced plasmas was initiated in the 1970s and reported by several laboratories using infrared pulse lasers.^{1–3} These early stages of the investigation concentrated mainly on the observation of keV-order photons and the identification of line emission from excited ions along an isoelectronic sequence.^{4–6} Several atomic models were developed to explain the characteristics of the emission spectrum.^{7–9} Most of them assumed homogeneous plasma volume of constant density and temperature. However, in laser plasmas the emission from any volume element is affected by conditions elsewhere in the target. In addition, there are steep density gradients and transient plasma conditions due to short hydrodynamic time scales. Recent development of high-energy laser technology provides the opportunity to demonstrate the scientific feasibility of laser fusion. It is becoming general understanding that x-ray generation, especially in the soft-x-ray region, in a laser irradiated pellet plays an important role as an efficient energy carrier.^{10–12} In addition, the uniform compression of the pellet may be more easily achieved with the help of x-rays.¹³

In the last few years it has been demonstrated that for short-wavelength laser irradiation of solid targets, the transport of energy into dense plasma regions occurs more efficiently.^{14,15} In this situation, the emission of soft x rays by an overdense target plasma also becomes more efficient, especially for high- Z material.¹⁶ X-ray conversion efficiency has been measured at 0.5 μm wavelength at average intensities from 3×10^{13} to 5×10^{15} W/cm².¹⁶ Similar experiments have been conducted at 10 μm ,¹⁷ 1.05 μm , 0.53 μm , and 0.35 μm ,¹⁸ and produced conversion efficiencies by assuming a blackbody spectrum. This resulted in the laser-intensity dependence of radiation tempera-

ture. Extensive investigation on overall characteristics of 0.53- μm laser-produced Au plasmas has been reported by Mead *et al.*,¹⁹ but the detailed dynamical behavior of emission and the optical thickness of the plasma were not discussed. Z dependence of the x-ray conversion efficiency has been studied experimentally to some extent by Gilbert *et al.*²⁰ but their photon energy range was limited only to the range over 0.7 keV. The absolute spectral intensity was determined indirectly by iteratively comparing the diode signals with a trial spectrum. Recently, the interaction between intense soft-x-ray radiation and solid matter has been investigated by the authors.²¹ They found that the interaction is extremely important to inertial-confinement fusion and thus parametric information including accurate spectrum, Z dependence, etc., is required. Furthermore, such intense x radiation is a promising candidate for the pump of an extreme ultraviolet (xuv) laser or as an exposure source for x-ray lithography.

In these plasmas the calculation of line transport is essential to understanding the physics. A number of papers have addressed nonlocal thermodynamic equilibrium (non-LTE) line transport for astrophysical low- Z hydrogen plasmas.²² In laboratory plasmas, the x-ray spectrum from medium- Z (e.g., Al) plasmas has been analyzed by solving rate equations for atomic processes and overall transport without the assumption of LTE.²³ But there are few works on x-rays from high- Z plasmas in a high-density region under the non-LTE assumption.

This paper presents x-ray spectra in the soft-x-ray region. The energy conversion efficiency is measured without assuming blackbody emission. The dependences on atomic number and laser intensity are also reported. By comparing the obtained results with non-LTE computer simulations, the emission characteristics coupled with hydrodynamic ablation processes are better understood.

II. EXPERIMENTAL CONDITION AND DIAGNOSTICS

0.53- μm light from a frequency-doubled GEKKO-IV laser with an energy of 4–20 J in 0.1, 0.15, 0.25 (short pulse), or 1.0 nsec (long pulse) full width at half maximum (FWHM) was focused onto the target through an aspheric lens of an effective f number of 1.6 with a nominal incidence angle of 54° . The irradiations were done near S polarization. The intensity distribution in the target plane was observed using a beam-monitor system that consists of a microscopic objective lens and a television camera. The image plane was varied along the laser-beam axis so that the intensity distribution was determined as a function of displacement from the best focus. We found the pattern to be reproducible from shot to shot. Since we were operating the GEKKO-IV laser system far below its design power, there was no nonlinear beam propagation in the laser glass, so the beam quality did not vary appreciably with laser power. The distribution is primarily due to intensity-independent aberrations and to diffractions. Figure 1(a) shows a typical intensity image of the 0.53- μm laser pulse at 200 μm in focus. Figure 1(b) shows the intensity profile of the above image. The profile had a modulation of about $\pm 30\%$ at an average intensity of 10^{14} W/cm^2 . We did not observe appreciable change in the distribution for short and long pulses. It was within the above modulation value.

The pulse duration and shape were observed using an optical-streak camera and/or monitored by a fast-response biplanar photodiode. The shape was determined to be roughly Gaussian.

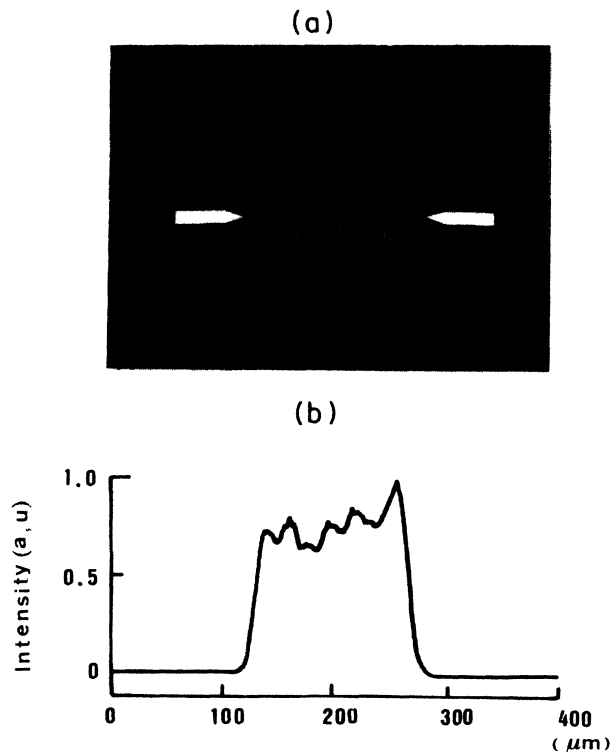


FIG. 1. (a) A typical intensity image of the 0.53- μm laser pulse in the target plane. The average intensity is 10^{14} W/cm^2 . (b) A profile of the laser intensity in the target plane.

The experimental setup is shown in Fig. 2. To monitor the emission image of the x ray above 1.5 keV, two x-ray pinhole cameras with a 7–8- μm pinhole diameter and a 55- μm -thick beryllium filter were mounted tangential to the target surface and at 45° from the target normal, respectively. Kodak XRP-5 films were used to record the x-ray images. The Be-filtered x-ray pinhole camera showed an amplitude modulation of about 15% in its x-ray micrograph of gold target. The modulation was found to roughly correspond to the intensity modulation in the incident laser beam, but the former was somewhat smoother than the latter. This difference is likely due to the large incidence angle of the laser beam. Lower- Z targets showed smoother x-ray emission profiles. At the incident angle used, the laser spot has an approximately elliptic shape whose eccentricity a/b is about 1.8 where a and b are the major and minor axes, respectively. The lengths of the axes estimated from the obtained x-ray micrographs were in good agreement with that calculated from the laser focusing position and the f number of the lens, taking into account the variation of the laser absorption rate in this spot. The maximum-minimum ratio of the laser intensity variation in the spot is estimated to be 2–3. We use hereafter the value \sqrt{ab} as the nominal laser-spot diameter for convenience to express the dimension of the spot at the target surface. This nominal laser-spot diameter was varied from 90 to 330 μm to obtain an intensity range 2×10^{13} – 2×10^{15} W/cm^2 . Typically it was fixed at 150–180 μm at $I_L \sim 2 \times 10^{14}$ W/cm^2 .

In the 0.15-nsec pulse experiments on gold targets, the underdense corona plasma was observed from the tangential direction by optical shadowgraphy using a synchronized probe beam (633 nm) of 60 psec pulse duration. Flash x-ray backlighting was separately used to observe tangentially the high-density region of the target with 1.4-keV x-ray photons in the short-pulse experiments. Expanding ions were always monitored using charge collectors, which were placed typically at 42° to the target normal.

Charge collector signals from the gold target showed an expansion velocity of 7×10^7 cm/sec for the maximum laser intensity investigated with a 0.15-nsec pulse. This

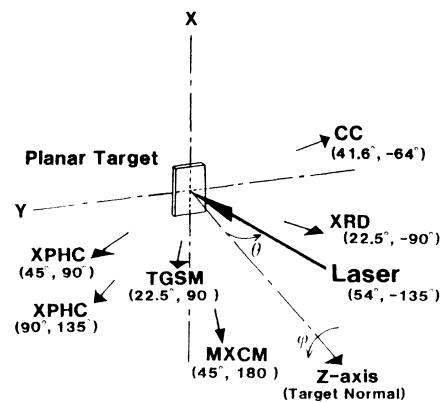


FIG. 2. The experimental setup for x-ray radiant energy measurements. Each diagnostic tool was mounted at an angular position (θ, φ) , where (θ, φ) are polar coordinates and a Z axis is on the target normal.

value is in agreement with that derived from the time-resolved optical shadowgram of the expanding plasma. At maximum laser intensity the velocity u corresponds to a coronal plasma temperature of 1.5 keV obtained from the relationship of $u \sim 2C_s/(\gamma - 1)$, where C_s is a sound velocity and γ is $\frac{5}{3}$.²¹

The expansion velocity of the high-density region was found to be 1.4×10^7 cm/sec for the 0.15-nsec pulse using the x-ray backlighting image. The x-ray image of the tangential pinhole camera showed the emission region of x rays above 1.5 keV expanded during laser-pulse duration by no more than 25 μm from the original target surface, even with the long pulse. From these experimental data, it is concluded that the overdense and low-temperature region did not expand more than 25 μm during a soft-x-ray emission time, which is less than one-fourth of the focal-spot diameter used.

Filtered seven-channel, absolutely calibrated x-ray *p-i-n* diodes were occasionally used to monitor the electron temperature of the coronal plasma using the Ross filter method and also used to estimate the level of hot electrons.

We used a soft-x-ray transmission grating spectrometer to obtain an x-ray spectrum profile in 0.1–2.0-keV range.²⁴ The dispersive element was a linear array of 0.3- μm -thick gold bars with 1 μm spatial period in a free-standing structure. The spectral resolution is estimated to be about 5 Å for the case of a 100- μm x-ray source size. The dispersed x ray was usually recorded on Kodak Type 101 film and also on Kodak NS-5T film when an $h\nu > 1$ -keV range of higher sensitivity was required. This spectrometer was mounted at 22.5° from the target normal. Typical x-ray emission spectra obtained using the transmission grating spectrometer are shown in Fig. 3. The Au planar target was irradiated in a 150- μm focal-spot diameter by a 1.0-nsec pulse laser. The film sensitivities are not calibrated. Three obviously recognizable band structures consisting of $h\nu = 0.15$ keV, 0.2–0.3 keV, and 0.6–1.2 keV can be seen. At the 0.12-nsec pulse with higher intensity $\sim 10^{15}$ W/cm², another hump was observed in the spectral range $\gtrsim 2.0$ keV on the Kodak NS-

5T film. The transmission grating spectrometer with the Kodak 101 film was also used to see the spectral-resolved size of the emission region by placing a pinhole of 150 μm diameter in front of the grating. A one-dimensional spatial image of the emission region, taken by the spectrometer with the input pinhole, showed a slightly larger size for the $h\nu \leq 500$ -eV region than that by the Be-filtered x-ray pinhole image. No significant difference was found in the emission sizes for the sub-keV range investigated. Although the accuracy is limited by the pinhole diameter, it is concluded that they coincide with the laser-spot size.

Filtered ten-channel biplanar x-ray diodes (XRD's) and four-channel x-ray calorimeters were used to measure the absolute x-ray radiant energy from the target. The XRD's had Al photocathodes whose quantum efficiency was measured by Day *et al.*²⁵ The filter sets used in the present experiment are listed in Table I with the absorption edges²⁶ utilized. The parylene and trichloroethylene films were made by the chemical vapor deposition (CVD) method and plasma polymerization with a thickness accuracy of $\pm 1.5\%$. The other metal layers were formed by a vacuum evaporation method with a nominal deposition accuracy of 120 Å. The spectral responses and typical combinations of channels used to deduce the data by the differential method for a programmed energy window are shown in Fig. 4. The diode itself had a rise time of about 34 psec. The signals of the XRD were monitored with the combination of Tektronix 7104 and 485 oscilloscopes. The temporal response of the 485 was not enough, therefore its signal response was calibrated using the 7104 whose response was about 350 psec.

The XRD's signal showed the x-ray emission time was nearly equal to the laser-pulse duration for 1 nsec and slightly shorter at higher-energy photon channels, but it was only ascertained to be less than 500 psec for short laser pulses because of overall temporal response of the detection. The XRD signal was time integrated to obtain the total electrical charge produced at the diode cathode taking into account a calibrated value of a cable attenuation and oscilloscope responses. The temporal stability of the photocathode's quantum efficiency was checked by comparing the signals of two XRD's with identical filters at the same target shot: one of which was preserved in a vacuum desiccator for five days after being aluminum-coated on the electrode and installed in the target chamber; the other had been used in the target chamber for four months to receive about 70 laser shots and was repeatedly exposed to air during this period. The quan-

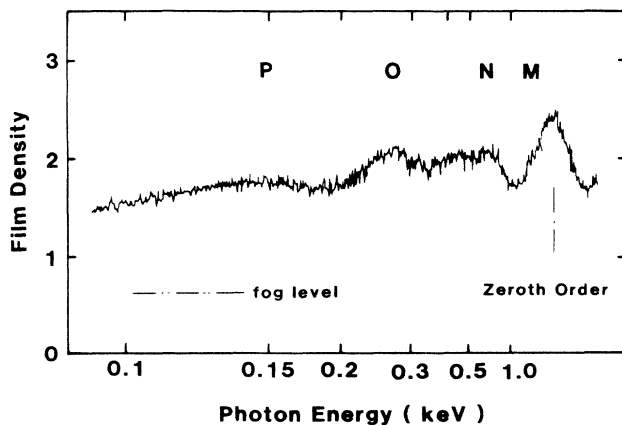


FIG. 3. Typical x-ray emission spectra in transmission grating spectrometer at a viewing angle of 22.5°. Au target was irradiated at $I_L = 7.3 \times 10^{13}$ W/cm² in 1.0 nsec.

TABLE I. Filter sets for XRD.

1.	$\text{C}_2\text{HCl}_{1.8}(0.88 \mu\text{m}) + \text{C}_8\text{H}_7\text{Cl}(0.1 \mu\text{m}) + \text{C}_8\text{H}_8(0.48 \mu\text{m})$
2.	Parylene (C_8H_8)(2 μm)
3.	V(0.37 μm) + C_8H_8 (0.5 μm)
4.	C_8H_8 (7.4 μm)
5.	Fe(0.5 μm)
6.	Fe(0.5 μm) + C_8H_8 (0.75 μm)
7.	Ni(0.37 μm) + C_8H_8 (0.5 μm)
8.	Zn(0.42 μm) + C_8H_8 (0.5 μm)
9.	Al(1.0 μm) + C_8H_8 (0.5 μm)
10.	Be(45 μm)

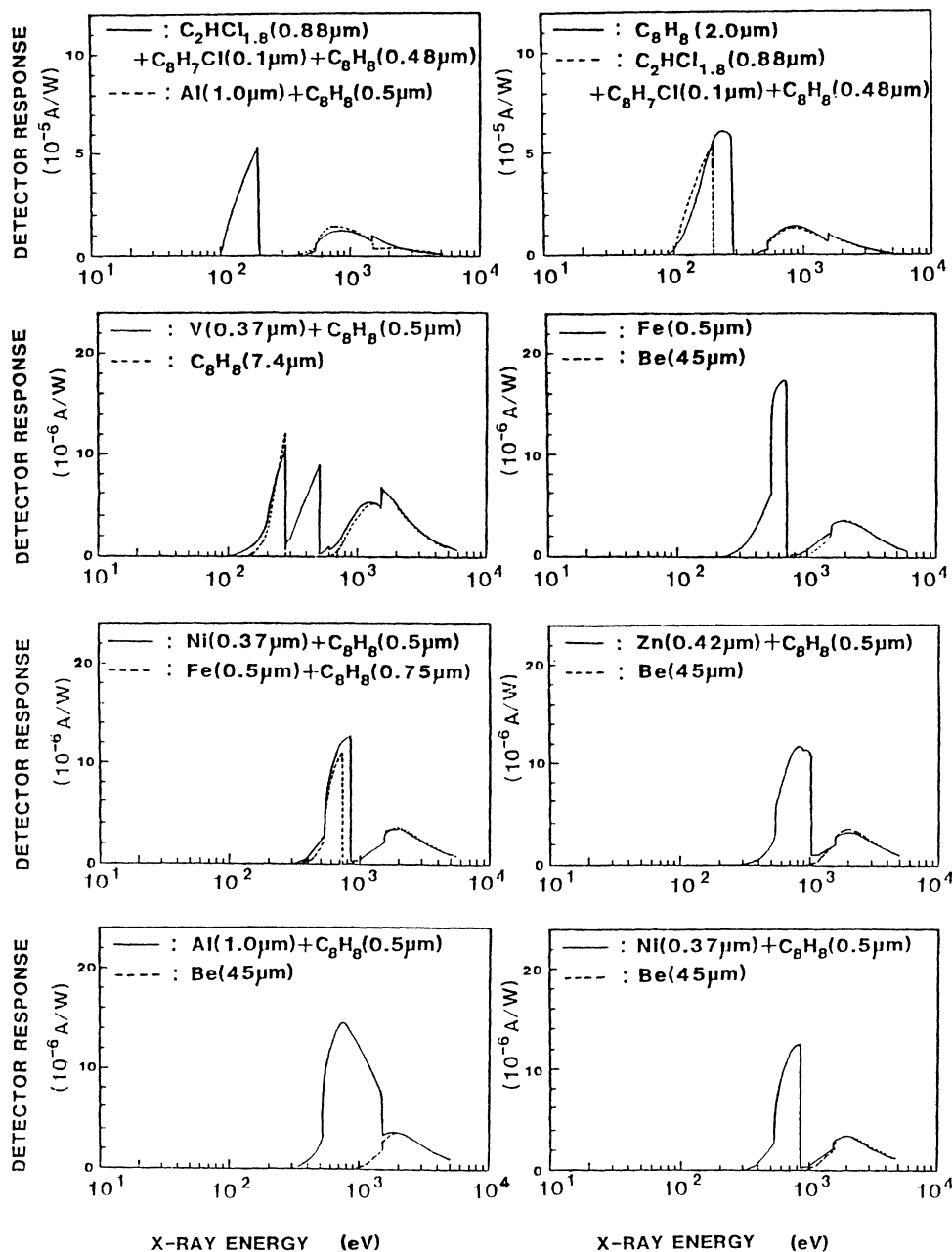


FIG. 4. Overall detector responses of filtered XRD's as a function of photon energy.

tum efficiency of the older photocathode was reduced by about 20%.²⁷

The evaluation of the absolute radiant energy was primarily carried out by differentiating the signals of the paired channels described in Fig. 3. The energy fluxes were obtained in the respective window of the photon energy. The problem in such a differential method is that the effective spectral response S_v in the respective energy window is not an ideal rectangular function, but a photon-energy-dependent function within the window. Furthermore, some excess response remains outside the desired window when the fitting of the responses of the two channels concerned is not perfect. Although we care-

fully designed the set of the filters so as to minimize the errors in the data deduction, these defects are inherent to such a differential method and it is inevitable to suffer from intolerable errors if the data deduction is carried out with the simple differentiation alone. However, the uncertainty in the x-ray radiant energy evaluation by the XRD's signal data can be considerably reduced by comparing it with the spectral shape in Fig. 3. The absolute spectral response of the Kodak 101 x-ray film is not known and the film gamma value is generally a function of the photon energy, but it is reasonably approximated to a constant value within a relatively narrow energy range of concern. The film gamma has different constant

values for respective photon-energy ranges. Thus the effective S_v in the data deduction is determined by referring to the profile of the film exposure at the energy band of concern without assuming a spectral response of rectangular shape. The differential of the XRD's signals obtained is equal to the convolution of the spectral response of the XRD's in Fig. 4, and the real x-ray spectrum profile in the photon-energy range of concern which is now derived by the transmission grating spectrometer. In order to assess the accuracy of the above procedure we checked the proportionality at several photon-energy ranges between the x-ray fluence deduced from the XRD's signals and that from the film exposure spectrally integrated. The slope of the proportionality is a function of the gamma value in the photon-energy range of concern. The experimental data were obtained for different x-ray spectrum shapes, thus different x-ray fluences at a specified range, which were achieved by using target materials of several atomic numbers. The proportionality of the two kinds of energy fluences was ascertained within the deviation of $\pm 10\%$ at the fluence region observed, even when different spectrum shapes were analyzed. It should be noted that these relations, in turn, provide the absolutely calibrated film response for different wavelengths in the sub-keV range. A similar procedure was done to eliminate the excess responses outside the desired energy band. The total error is caused by the uncertainty in the filter thickness and the error in the evaluation of the effective S_v .

The signals of the parylene channel at two different angular positions indicated an approximate cosine distribution at $I_L = 5 \times 10^{13} - 4 \times 10^{14} \text{ W/cm}^2$. The zinc channel showed a nearly isotropic angular distribution rather than a cosine distribution.

III. RADIANT ENERGY SPECTRUM FROM Au PLASMAS

Figure 5 shows typical radiant energy spectra obtained at 100-psec and 1.0-nsec laser pulses. The horizontal bars of the data points correspond to the observed energy band. It is found in Fig. 5 that the obtained spectral shape is not of the ideal blackbody spectrum type and most of the radiant energy is concentrated below 0.7 keV. Shorter pulses produced relatively smaller radiant energy and clearly showed a dip at 300–500 eV. Longer pulses produced larger radiant energy. Relatively large energy transport from a laser-heated region to an x-ray-emitting region may be responsible for this; at short pulses smaller electron conduction may exist. These facts will be compared with the simulation and their origin will be discussed in Sec. V. The observed humps in the spectrum are explained by a non-LTE average ion model simulation. The open circles show the data by Mead *et al.*¹⁹ Their data were plotted after the nominal translation of the laser incidence angle θ taking into account the laser bulk absorption change and their observation angle.^{19,28} The present result is in reasonable agreement with their result except for the 600-eV range—if one considers that both results have error bars, and the observation angles to the target normal are not identical. Unfortunately, they did not provide the spectral intensity at the photon energy

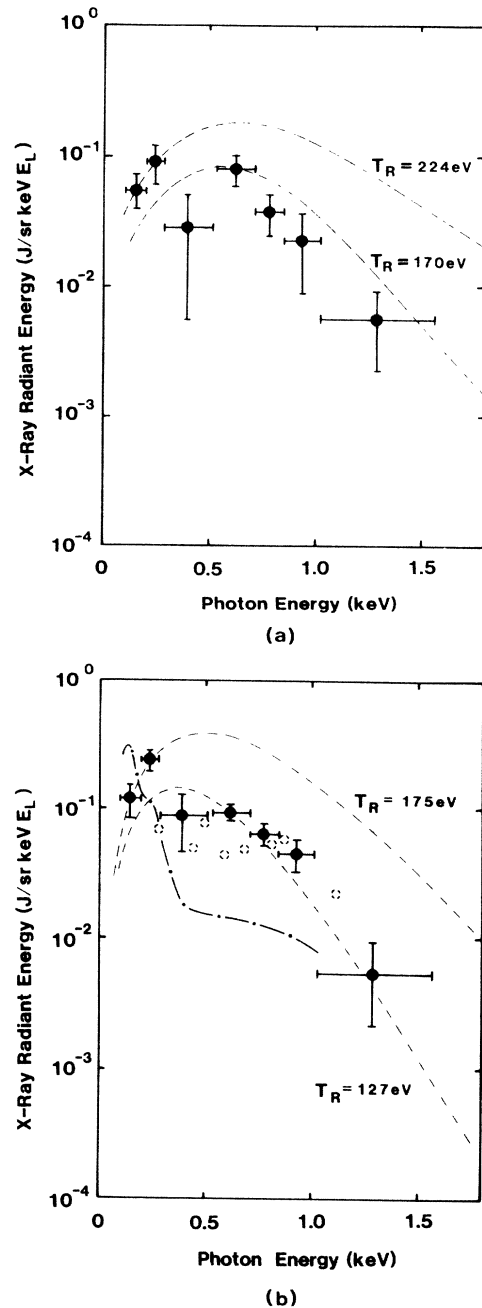


FIG. 5. Radiant energy spectra from Au plasma at a viewing angle of 22.5° at (a) $I_L = 4.0 \times 10^{14} \text{ W/cm}^2$ in 100 psec and (b) $1.0 \times 10^{14} \text{ W/cm}^2$ in 1.0 nsec. Dashed lines show blackbody radiation spectra. Open circles show the data by Mead *et al.*¹⁹ and a dotted line shows the data by Ceglio *et al.*²⁰

less than 250 eV where considerable radiant energy concentrates. The dotted line shows the data from the soft-x-ray streak camera coupled with a transmission grating by Ceglio *et al.*²⁹ The streak data were unfolded using the overall spectral response of the detection system. We do not understand, as yet, why considerable difference in their spectra was obtained with nearly identical experimental conditions at the same laboratory.

The present results clearly show that the spectrum deviated from the blackbody spectrum, especially for laser-pulse durations of less than 0.25 nsec. The spectra approach the blackbody-radiation spectral shape as the pulse increases to 1 nsec, but deviation still remains. The radiation temperature T_R used to achieve the radiation energy level obtained at $h\nu=250$ eV for the short pulse is estimated from the blackbody relation to be 224 eV. On the other hand, the nominal T_R used to explain the data point at $h\nu=600$ eV is 170 eV. These values are 175 eV and 127 eV for a 1-nsec pulse, respectively. The dashed lines in Fig. 5 shows the blackbody-radiation spectral profile for respective radiation temperature for comparison. In these calculations, the emission area was estimated from the x-ray image of the Be-filtered x-ray pinhole camera and that of one-dimensional spatial-resolved transmission grating spectrometer. The target area irradiated with lower intensity than usual may emit the softer x-ray whose spectrum maximum concentrates in the range less than 250 eV and may enhance the spectral part of about 250 eV or less. But this does not seem to be the main cause for the present spectra, because the nominal irradiated area determined by the simple laser ray trace is in good accord with the maximum size of the emission at $h\nu\sim 100$ eV as described in the previous section. The ratio of the areas emitting 100- and 600-eV photons was found to be less than a factor of 2 at most. The above area ratio cannot explain the difference in the radiation temperatures estimated at the lower and higher photon-energy regions if we follow the equation $J_R = cU_\nu(T_R)S/4\pi$, where J_R is the blackbody radiant energy flux per unit frequency interval from an area S , $U_\nu(T_R)$ is the Planck function with an equilibrium temperature T_R and c is the speed of light. In addition, the x-ray spectrum profile did not change significantly at the nominal laser intensity from $\sim 10^{13}$ to 4×10^{14} W/cm².

In separate experiments, the filtered seven-channel x-ray *p-i-n* diode array produced absolute spectral intensity in the photon-energy range of 1–22 keV at Au targets. The x-ray intensities were 10^{14} , 10^{10} , and less than 10^8 keV/keV sr at $h\nu=1$, 7, and 22 keV, respectively, at the laser intensity of 10^{14} W/cm². The measured x-ray fluence at the above intermediate photon energies is a superposition of free-bound emission from cold electrons and of bremsstrahlung radiation generated by hot electrons as they slow down in the overdense plasma. Order-of-magnitude estimates of the amount of energy in the hot electrons that would produce the observed hard-x-ray fluence can be made by assuming that the radiation is produced by thick-target bremsstrahlung radiation from a Maxwellian hot-electron distribution. To minimize the thermal-emission background by the cold electron, we use the x-ray fluences at the two highest energy channels to infer a hot-electron temperature. Thus the temperatures of the cold electron and hot electron are estimated to be 0.6 and 4.6 keV, respectively. The fraction of a hot-electron number density to a critical number density is also estimated to be 1.7×10^{-3} . In this estimation we used Eq. (5.15) of Ref. 30 and took an electron stopping range multiplied by the laser-spot area as an emission volume.

The heat-flux density by electron is roughly proportional to $n_e(kT_e)^{3/2}$ where n_e is an electron density, then the ratio of the heat flux by hot electrons to that by cold electrons is of the order of 10^{-3} . This value is quite low and it is in agreement with the value estimated by the Appendix in Ref. 2. This order of magnitude of the level of the hot-electron generation is also suggested by the charge collector signal which did not show any significant fast-ion peak in its time-of-flight spectrum. However, the hot electron may produce x ray efficiently because of its high energy. The collisional ionization and excitation rates by the electron are proportional to $n_e \exp(-h\nu/kT_e)$ in a Maxwellian distribution, where $h\nu$ is the relevant excitation energy that is approximately equal to the photon energy. Then the ratio of the collisional ionization and excitation rates by the hot electron to that by the cold electron is determined to be 10^{-4} for the photon-energy range of less than 600 eV. These ratios estimated above are too small to claim that the hot electron is a main source in producing the deviation from the blackbody emission.

From the above discussion we conclude that the emission observed at 0.1–1.6 keV cannot be described either by the blackbody radiation with a single radiation temperature or by the hot electron. This cannot be explained by the two-dimensional effect, because the emission sizes for 100–800 eV were found to be almost identical to the laser-beam spot sizes used. Therefore, the large lower-temperature region which will preferentially contribute to the 100–300-eV photon emission did not exist around the beam spot on the target. The obtained results suggest that the observed feature of the spectrum is inherent in the emission process.

The other approach to explain these experimental results is to consider the axially projected structure of the emission in the plasma; the optical thickness will not be sufficient to guarantee blackbody radiation for all the photon energies investigated. Lower-energy photons may be produced at the high-density plasma region which may be optically thick enough to provide a cosine angular distribution. The optical thickness will be very roughly estimated by using the Rosseland mean free path for bound-free transition,³⁰

$$\lambda_R \sim \frac{92.5}{N^2} \frac{T_e^{3/2} T_R^2}{\langle Z \rangle (\langle Z \rangle + 1)^2} \text{ cm},$$

where N is the ion density in 5×10^{22} cm⁻³, T_e and T_R are the electron and radiation temperature in keV, respectively, and $\langle Z \rangle$ is the average ionization charge. At $T_e \sim T_R = 200$ eV, $N = 5 \times 10^{21}$ cm⁻³, and using the approximate relation $\langle Z \rangle = \frac{2}{3} (AT_e)^{1/3}$,⁷ λ_R is estimated to be 40 μm . The value is larger than the plasma scale length. However, for bound-bound transitions which are dominant for high- Z targets, the plasma will be optically thicker for the photons of $h\nu \lesssim 200$ eV. Such a situation may not apply to the emission of $h\nu > 500$ eV. If the plasma is optically thin, then the emissivity decreases and the angular distribution approaches an isotropic one. This situation seems to be responsible for the present results. These explanations are supported by the computer-code simulation described later in Sec. V.

For comparison, we made intentionally nonuniform irradiation on gold targets by putting a concentric structured mask in the laser-beam path in front of the final focusing lens. In this case, a very rough estimate of the scale length of nonuniformity was $30\ \mu\text{m}$. We found that the structured laser-beam profile enhanced the radiant energy at 200–300 eV by a factor of 2 at shorter laser pulses compared to the smooth laser-beam profile under the same average laser intensity. This may suggest that the plasma region where the quasiblackbody condition is attained becomes hotter at the peak locations of the laser intensity modulation so that the emissivity is enhanced there and/or the effective emission surface are increases due to nonuniformity of plasma expansion.

At normal incidence, the radiant energy increased compared to 54° incidence angle. This is inferred to be due to the increase in the plasma density by a factor of 3 at which the laser energy is deposited, resulting in the increase of laser absorption. In this situation plasma density and temperature may have a different profile from that with the 54° incident angle so that energy transport to the x-ray-emitting region becomes more effective.

IV. LASER INTENSITY DEPENDENCE OF X-RAY CONVERSION EFFICIENCY IN Au PLASMAS

The conversion efficiencies from the incident laser energy to the total emitted x-ray radiant energy by 0.1–1.6 keV have been obtained as shown in Fig. 6 by integrating spectral radiant energy such as Fig. 5. We did not obtain the angular distribution over the whole energy range, so it is rather difficult to estimate the complete sets of uncertainty in the whole x-ray $h\nu$ region to deduce the uncertainty of the conversion efficiency. Here we assumed from the data of the parylene channel XRD that the emission angular distribution follows cosine law for the whole $h\nu$ region investigated. This does not hold to the photons of around $h\nu \sim 1\ \text{keV}$, which showed a distribution approximating the isotropic one. But the error induced in the total conversion efficiency by the ambiguity in their angular distributions is relatively small ($\sim 15\%$) because the radiant energy at $h\nu > 1\ \text{keV}$ is much smaller (10%) than that at $h\nu = 100\text{--}600\ \text{eV}$. The angular distribution obtained for lower energy range in the present experiment is consistent with the result by Mead *et al.*⁴⁰ In the long-pulse irradiations, the conversion efficiency is about 40%—a value two times as large as that for the 0.25-nsec pulse at the intensity of $\sim 10^{14}\ \text{W/cm}^2$. This means that the increase in plasma scale length at longer pulses and the increase in laser absorption³¹ both may have contributed to the increase in the x-ray conversion efficiency as discussed in the next section. Figure 6 shows that the conversion efficiency is only weakly dependent on I_L . At higher laser intensity, $6 \times 10^{14}\text{--}2 \times 10^{15}\ \text{W/cm}^2$, the spectral intensity around 1 keV increased by a factor of 2,

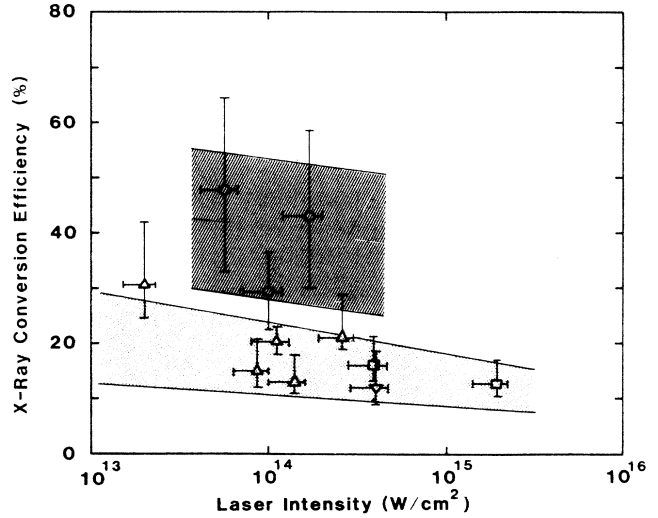


FIG. 6. Laser-intensity dependence of x-ray conversion efficiency for various laser-pulse durations: \circ , 1.0 nsec; \triangle , 0.23–0.25 nsec; \square , 0.15, nsec; ∇ , 0.1 nsec.

compared to that at $I_L \sim 1 \times 10^{14}\ \text{W/cm}^2$, but lower-energy photons still dominate in energy flux. At these laser intensities the classical absorption becomes less effective because of higher plasma temperature. This probably causes the decrease in x-ray conversion efficiency as shown in Fig. 6, while higher-energy photon emissions increase due to the higher plasma temperature at the underdense plasma region. From the beryllium-filtered x-ray calorimeter's signal, the total energy above 1.6 keV was estimated to be less than 1% of the incident laser energy at the laser intensities investigated.

V. COMPUTER SIMULATION

The x-ray emission spectra obtained have been investigated by the one-dimensional hydrodynamic Lagrangian code HIMICO (Refs. 32 and 33) which is coupled with a non-LTE average ion model and multigroup radiation transport. In order to describe the plasma x-ray which was inferred in the previous sections to be generated in a variety of density regions and times in nonstationary plasma hydrodynamic motion, we need to analyze the system under the nonlocal thermodynamic equilibrium which is valid for wide density and temperature ranges. An LTE model is valid only in the region where collisional transitions overwhelm radiative transitions, so the density required to achieve LTE in an optically thin plasma is quite high.³⁵ The radiation transport calculation incorporates the emissivity and absorption coefficient of the medium, and hence needs the detailed information of the atomic-energy state.

We employ here the average ion model^{34,35} to describe the time evolution of electron population P_n with principal quantum number n . The population change in this model is given as follows:

$$\begin{aligned} \frac{d}{dt}(NP_n) = & R_n N_e N Q_n - I_n N_e N P_n + N \left[\sum_{m(>n)} A_{nm} P_m Q_n - \sum_{m(<n)} A_{mn} P_n Q_m \right] + \sum_{m(>n)} C_{nm}^D N_e N P_m Q_n \\ & - \sum_{m(<n)} C_{mn}^D N_e N P_n Q_m + \sum_{m(<n)} C_{nm}^U N_e N P_m Q_n - \sum_{m(>n)} C_{mn}^U N_e N P_n Q_m, \\ Q_n = & 1 - P_n / g_n, \end{aligned}$$

where N , N_e , and g_n are the ion number density, free-electron number density, and statistical weight of the n th level, respectively. Here, R_n , I_n , A_{nm} , C_{nm}^D , and C_{nm}^U are the rate coefficients for recombination into the n th level, ionization from the n th level, Einstein's A coefficient, collisional deexcitation (from m to n), and collisional excitation (from m to n), respectively. The recombination rate R_n consists of the radiative, three-body, and dielectronic recombinations. The free-electron number density N_e is related with an average ion charge Z^* as

$$N_e = NZ^* = N \left[Z - \sum_n P_n \right].$$

The energy of bound electrons E_n is expressed to be

$$|E_n| = 13.6 \frac{q_n^2}{n^2} - \Delta E_n \text{ eV},$$

where q_n is the effective nuclear charge, e.g., the net nuclear charge as seen by electrons in the n th level, which is calculated with Mayer's screening constants σ_{nm} as $q_n = Z - \sum_{m=1} \sigma_{nm} P_m$.^{36,37} ΔE expresses a potential lowering by perturbers such as free electrons and neighboring ions. The pressure ionization effect is added to the calculation by forcing the degeneracy of the n th bound-electron shell to decrease to zero at a high-density limit; the electron populations around the valence shell ($r_n \simeq R_0$) are numerically modified so that the solution is close to the Thomas-Fermi-Dirac description in the high-density region. Here r_n and R_0 are the electron-orbital radius and ion-sphere radius, respectively.³⁵ Thus, unphysical and abrupt change in the population is avoided. Most of the rate coefficients are introduced from the lists by Post *et al.*³⁴ and the detailed balance.

To compare with the corona and LTE model calculations, the average ionization state of an aluminum plasma which is approaching an equilibrium state at $T_e = 100$ eV has been calculated to test this code as a function of the ion density. The result coincides well with the corona model and LTE calculations at low- and high-density limits, respectively, as shown in Fig. 7.³⁸ However, it should be noted that the deviation from the LTE model is signifi-

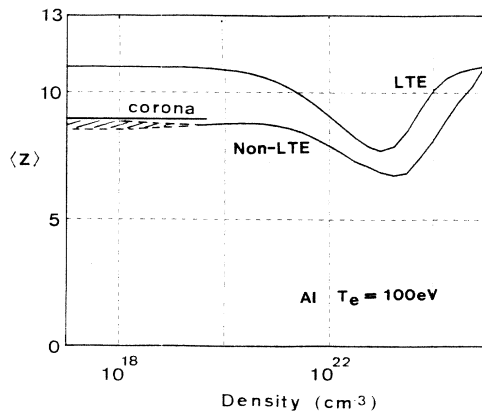


FIG. 7. Average ionization charge of aluminum plasma by non-LTE calculation as a function of ion density at ionization equilibrium in comparison with the corona and LTE model calculations.

cant at the ion density region of 10^{20} – 10^{24} cm^{-3} which is the most interesting region to laser-produced plasmas.

Before we start the calculation to simulate the experimental results described in Sec. III, we calculate the emitted power density as a function of plasma density N and temperature T_e to obtain a general feature of x-ray generation. Figure 8 shows the contour of total emitted power density $J(N, T)$ at $t = 500$ psec in a gold plasma. The solid lines indicate $J(N, T) = \text{const}$. These lines of $J(N, T) = \text{const}$ have a convex shape downwardly at higher temperature regions, as seen.³³ In a subsonic ablation region it is reasonable to assume that the plasma pressure $P = N(Z + 1)T_e$ has a constant value, therefore $NT_e^{4/3} = \text{const}$ using the approximate equation $Z \sim \frac{2}{3}(AT_e)^{1/3}$.⁷ When the parameters N and T_e changed according to $NT_e^{4/3} = \text{const}$, it is found that $J(N, T)$ has the maximum value because the line of $NT_e^{4/3} = \text{const}$ can be tangential to the line of $J(N, T) = \text{const}$. When the parameters N and T_e were changed according to $NZT_e = 7.8 \times 10^{24}$ eV cm^{-3} (or 12.5 Mbar), it was found that the total emitted power density $J(N, T)$ integrated from 0 to 2 keV has its maximum value at $N = 1.0 \times 10^{21}$ cm^{-3} and $T_e = 300$ eV due to the intense and numerous line emissions. This region is far from the validity domain of the LET model or the corona model. The reason for this maximum is very simple. In the lower-density side, the emission is proportional to the density. On the other hand, in the higher-density side, bound-bound emission is reduced in number of lines and finally vanishes because the higher levels disappear due to large potential lowering and low temperature.

The figure is useful in providing an idea of the region of emitted radiation. This contour of J at $t = 500$ psec agrees with the contour at $t = 100$ psec except at a density lower than $N \sim 10^{19}/\text{cc}$, and hence it is possible to predict the maximum value of total emission using this figure for any time longer than 100 psec.

The dielectronic recombination is also one of the important processes in laser-produced plasmas. Since the ionization state is reduced due to this process at a lower density region, the line-spectra shift towards a lower-

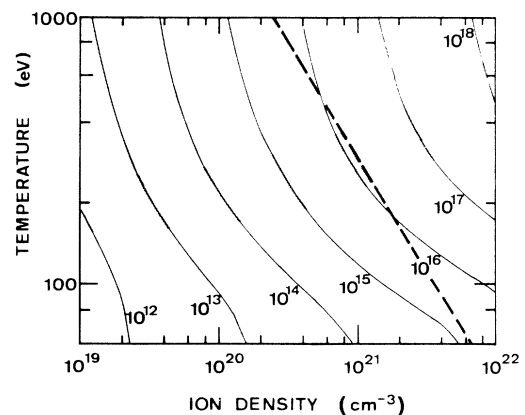


FIG. 8. Contour of total emitted power density $J(N, T)$ (W/cm^3) at $t = 500$ psec in a gold plasma. The maximum of total emission is shown by the shaded region for various choices of the product $NT_e^{4/3}$.

energy side and some of their intensities are larger than that in the non-LTE model without the dielectronic recombination process.³³

The calculation to simulate the experimental results assumed that a spherical target having a radius the same as a focal-spot radius³⁹ is irradiated by a 150-psec and 18.8×2 -J green laser whose incident angle is set to 54° in order to replicate the experimental incident angle. The one-dimensional calculation seems to be validated by the fact that lateral energy transport was not a major effect on the emission. The similar results on the x-ray images have been also obtained recently by Mead *et al.* who studied low- Z plasmas such as Be or Al.⁴⁰ However, the axially confined energy transport of the heated electrons into the overdense plasma appears inhibited and was claimed repeatedly in the studies of mass-ablation rate, pressure, etc.^{41,42} Here we set the flux-limitation factor f , which limits the energy transport caused by free-streaming electrons, to either 0.01 or 0.03. The fraction of resonance absorption is principally set to 0.03 of the laser energy which reached the critical density. This absorbed energy appears as the hot-electron energy. The detailed description of the hot-electron transport in our code is given in Ref. 32. The temperature of the hot electron is evaluated by Estabrook and Krueer's scaling law.⁴³ It is plausible that magnetic fields may be responsible for the flux limitation at such a finite-boundary geometry.⁴⁴

Figure 9 shows electron temperature and ion density profiles for $f=0.01$ at a laser peak for a 150-psec FWHM pulse. A steep profile is due to inhibited thermal-electron transport; in other words, the inhibition operates prominently in the steep-gradient region of the plasma produced by such a short laser pulse. A plateau is formed by radiation transport. This indicates radiative energy transport is essential in dense regions of high- Z plasmas free from such inhibition mechanisms which the electrons may be influenced by.

Figure 10 shows spectral power density of emitted radi-

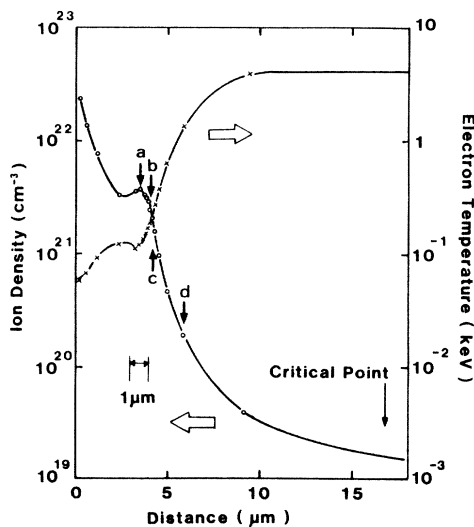


FIG. 9. Electron temperature and ion density profiles in ablated Au plasma at laser peak. Laser pulse is 150 psec FWHM and $E_L = 18.8 \times 2$ J.

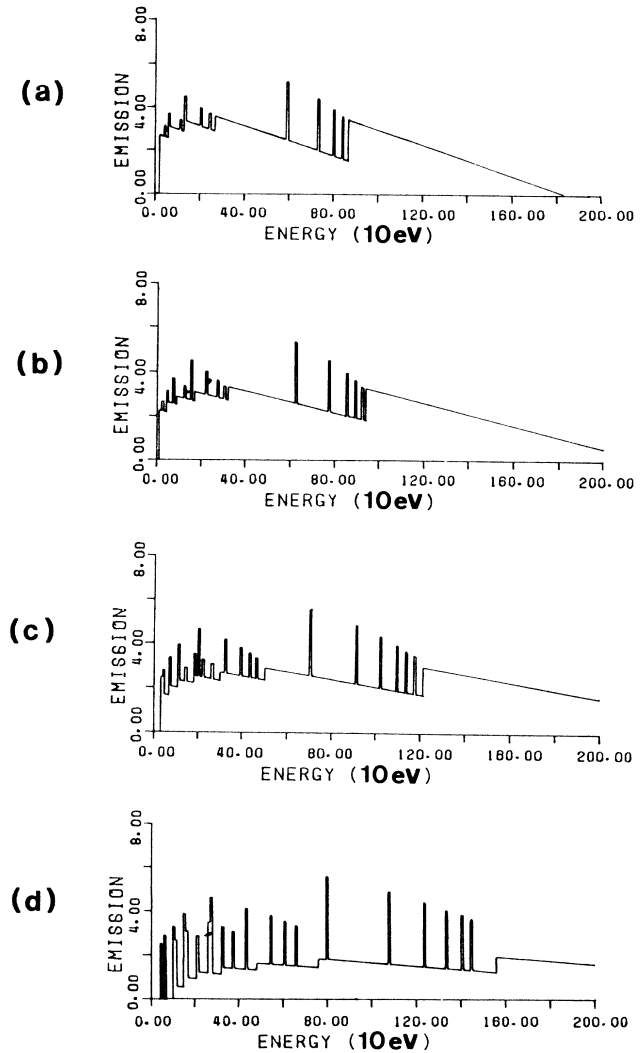


FIG. 10. Spectral power density of emitted radiation at the sampled points denoted by the arrows in Fig. 8. Vertical axis is in logarithmic scale and in arbitrary units.

ation at the sampled points denoted by the arrows in Fig. 9. Bound-free radiation is more sensitive to the temperature and density changes than bound-bound radiation. This trend is apparently seen in the line (~ 600 eV) emission from N shell: the line strength remains constant from $N_i = 4 \times 10^{21}$ to 4×10^{19} cm^{-3} . The bound-free emission less than 1 keV is large in the plateau region, while the line emission is dominant in the steep profile region. Since the line emission determines the total emitted power, its energy transport is one of the most important processes to determine the x-ray conversion efficiency. This is reflected in the conversion efficiencies at 1 nsec and 100 psec laser experiments. The simulations give efficiencies of 46.7% and 6.7% from laser to x ray, and efficiencies of 54.3% and 20.6% from absorbed energy to x-ray energy, for 1-nsec and 100-psec pulses, respectively. In the former case, the laser parameters are 17.9 J/nsec and 150- μm -diam focal spot, and in the latter case they are 10.6 J/100 psec and 184 μm . At longer pulse irradiation with the same laser intensity, the axial plasma scale

length is larger and then the laser absorption tends to increase. This increase in the laser absorption contributes to some parts of the increase in x-ray conversion efficiency. However, it should be noted that the region of steep density gradient is optically thin for $h\nu \geq 500$ eV because the line centers in the neighboring two regions have an energy difference larger than the linewidth and hence the opacity is mainly determined by bound-free opacity. On the other hand, the optical thickness λ_R at the plateau region is relatively large for $h\nu \sim 200$ eV although not sufficient to provide the blackbody condition $\lambda_R \ll L_p$, where L_p is a local plasma density scale length. Accordingly, for a longer pulse, the emission becomes larger because the density scale length is longer: the total energy of the emitted x ray is mainly given by the line emission and is determined by the volume emission process in the region giving a steep density gradient. Figures 9 and 10, furthermore, indicate that the sub-kilovolt x-ray emission levels are not significantly affected by the three-dimensional expansion of the underdense plasma because the x ray of concern is generated within several μm from the ablation region. This is consistent with the one-dimensional plasma model used in the present calculations.

The total emitted spectra for 1-nsec and 100-psec cases are shown in Fig. 11, where the corresponding experimental data are also shown. The spectrum for a 1-nsec pulse shifts a little towards the lower-energy side and is narrow for $h\nu \geq 500$ eV, compared to that for the 100-psec pulse. The lower (~ 200 eV) and higher (~ 700 eV) energy peaks mainly come from the bound-bound emissions into $n \geq 5$ level and $n=4$ level (N -shell), respectively. The line spectrum in the LTE model shifts towards the higher-energy side as compared to the non-LTE model, where the energy of the bound electrons becomes significantly higher for a highly stripped ion and hence a high-energy x ray is produced. This LTE result disagrees with the experimental result, in which the radiation energy above 1.6 keV was less than 1% of the incident laser energy.³³

The calculated spectra are in excellent agreement with the experimental results, especially for a short laser pulse at $f=0.03$ except for the lower-energy (~ 200 eV) component. The above results indicate that the level of the x-ray spectrum is closely related with the value of the energy-flux-limitation factor in an ablating plasma. As we described above, the increase in the calculated emission level originates in the increase in the density scale length at the steep-density-gradient region because the total emitted energy is determined by the volume emission process. Larger flux-limitation factor leads to larger emission volume near the ablation region. The flux limitation does not operate well at the longer-pulse irradiation because the density scale length is sufficiently long.

We investigated the effect of hot electron on the level of sub-keV emission and its spectrum. When we changed the fraction of resonance absorption at the critical density as a parameter from 0.03 to 0.10 in Fig. 11(b), the emission level at $h\nu=250$ eV increased by 17%. On the contrary, when the fraction decreased from 0.03 to 0.005, the emission level decreased by 6%. The spectrum profiles were almost identical at these fractions. It should be noted that the above change in the level of the hot electron

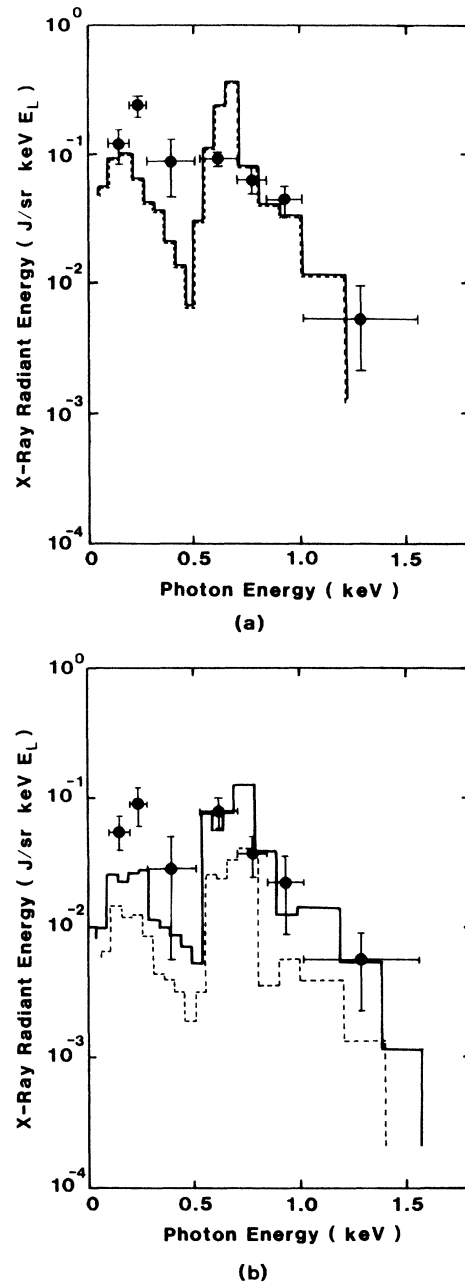


FIG. 11. Calculated emitted spectra of Au plasma for the (a) 1-nsec and (b) 100-psec cases. Solid circles show experimental values. Solid and dashed lines denote the results for $f=0.03$ and 0.01, respectively.

makes relatively little change in the emission level. We consider that the above result reflects that at the range of the present experimental conditions the plasma temperature-space distribution near the ablation region is dominated by the thermal-electron heat transport and the hot electron is not playing a critical role affecting the emission level. We could not observe the effect of laser and/or plasma microfilamentation of several-micron scale length on the emission spectrum, but it would be unlikely that such microfilamentation dominates the whole hydrodynamical structure of the plasma which determines the

ionization-emission dynamics, especially in overdense regions.

There are many possibilities which may improve the discrepancy between the experimental results and the simulation. One of these is the contribution from sublevel transitions which are neglected in the average ion model. The simulation cannot satisfactorily replicate the difference between 1-nsec and 100-psec pulses concerning the spectrum dip around 400 eV. The Stark broadening at $N_i \sim 10^{21} \text{ cm}^{-3}$ is about 20 eV and may not play an important role here. Because the energy window of the x-ray diode for each channel is wide, the direct comparison of the spectrum dip between the simulation and experiments requires a finer resolution of the spectrum.

The influence of self-generated azimuthal magnetic fields on the emission spectrum will be a subject for future investigation.

VI. Z DEPENDENCE OF X-RAY SPECTRUM AND CONVERSION EFFICIENCY

Similar x-ray generation experiments have been made with other solid target materials at $I_L = (1.0 \pm 0.2) \times 10^{14} \text{ W/cm}^2$ in 1.0 nsec, a laser spot of 150 μm diameter, and the incidence angle of 54°. The other target materials investigated are polyethylene, aluminum, titanium, copper, molybdenum, tin, gadolinium, dysprosium, and tantalum plates. Typical emission spectra are shown in Fig. 12. The target plates were carefully handled and/or chemical-

ly cleaned in order to keep the surfaces free from oxidation until laser irradiation. Gadolinium and dysprosium used in these experiments have been produced with a purity of 99.9% and sealed under argon gas in glass cells for a long storage period. Nevertheless, some oxidation could not be avoided as shown in an aluminum spectrum in which a small hump exists at 600–700 eV. This hump cannot be explained by the atomic structure of aluminum. The position coincides with the oxygen *K* lines. We conclude this hump is caused by the emission from the oxygen ions and its contribution to the total emission is of the order of ($10^{-3} \text{ J/sr keV } E_L$) or less for all other materials investigated. The oxygen emission is thus found to be in relatively much lower levels than that by other atomic elements in the present experiments.

Figure 13(a) shows x-ray conversion efficiency as a function of *Z*. The ordinate expresses the fractions of laser energy converted into x-ray energy per unit solid angle at the XRD detector array, which was angled to 22.5° from the target normal. One can obtain the total conversion efficiency easily by multiplying the angular distribution function. The efficiency is broken down into fractions corresponding to respective photon-energy ranges as indicated by several lines. The errors for the integrated efficiency value are about 20% for all elements. It should be noted that the integrated conversion efficiency increases gradually with some undulation as *Z* increases. In the fractional efficiencies in Fig. 13(a), undulation structure is more clearly seen. These undulations are due to

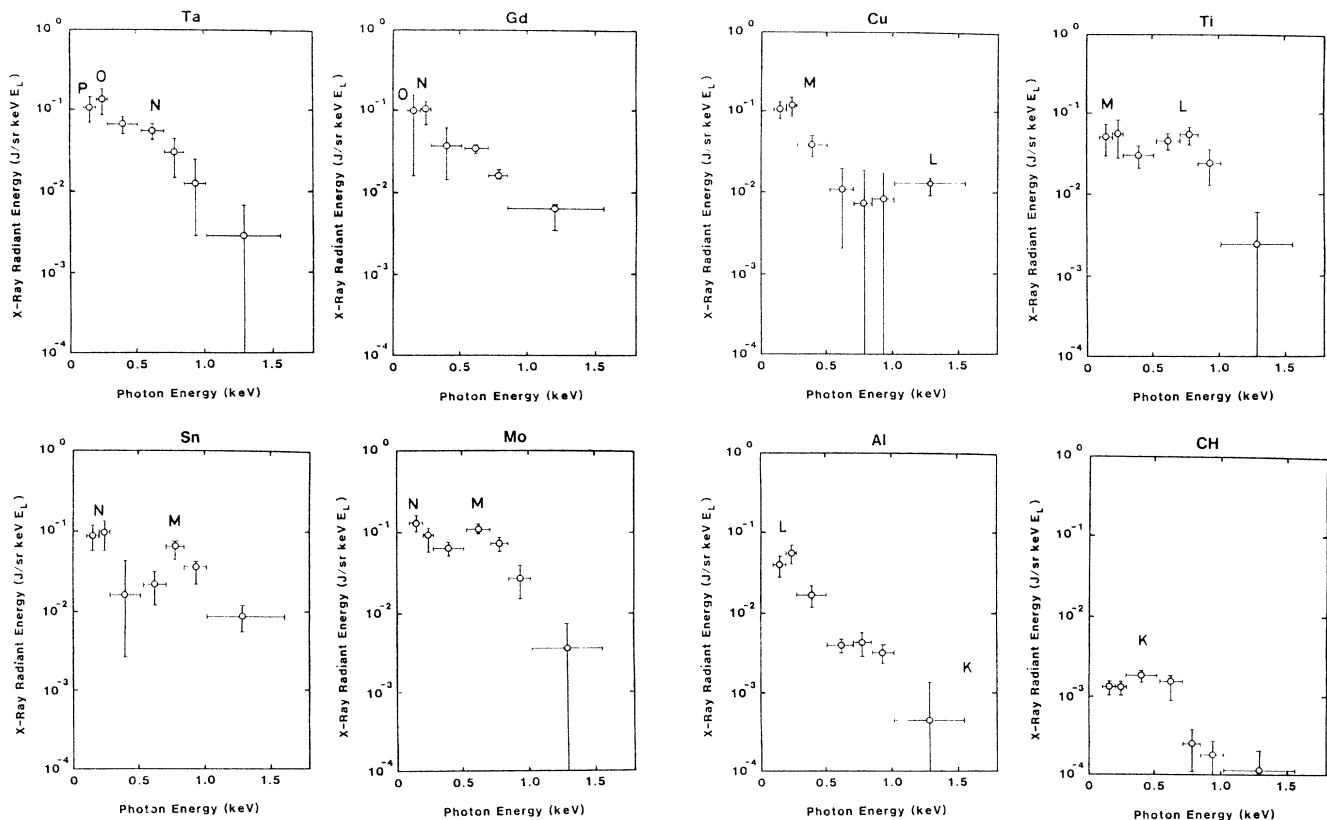


FIG. 12. Soft-x-ray emission spectra from various *Z* targets at $I_L = (1.0 \pm 0.2) \times 10^{14} \text{ W/cm}^2$ in 1.0 nsec.

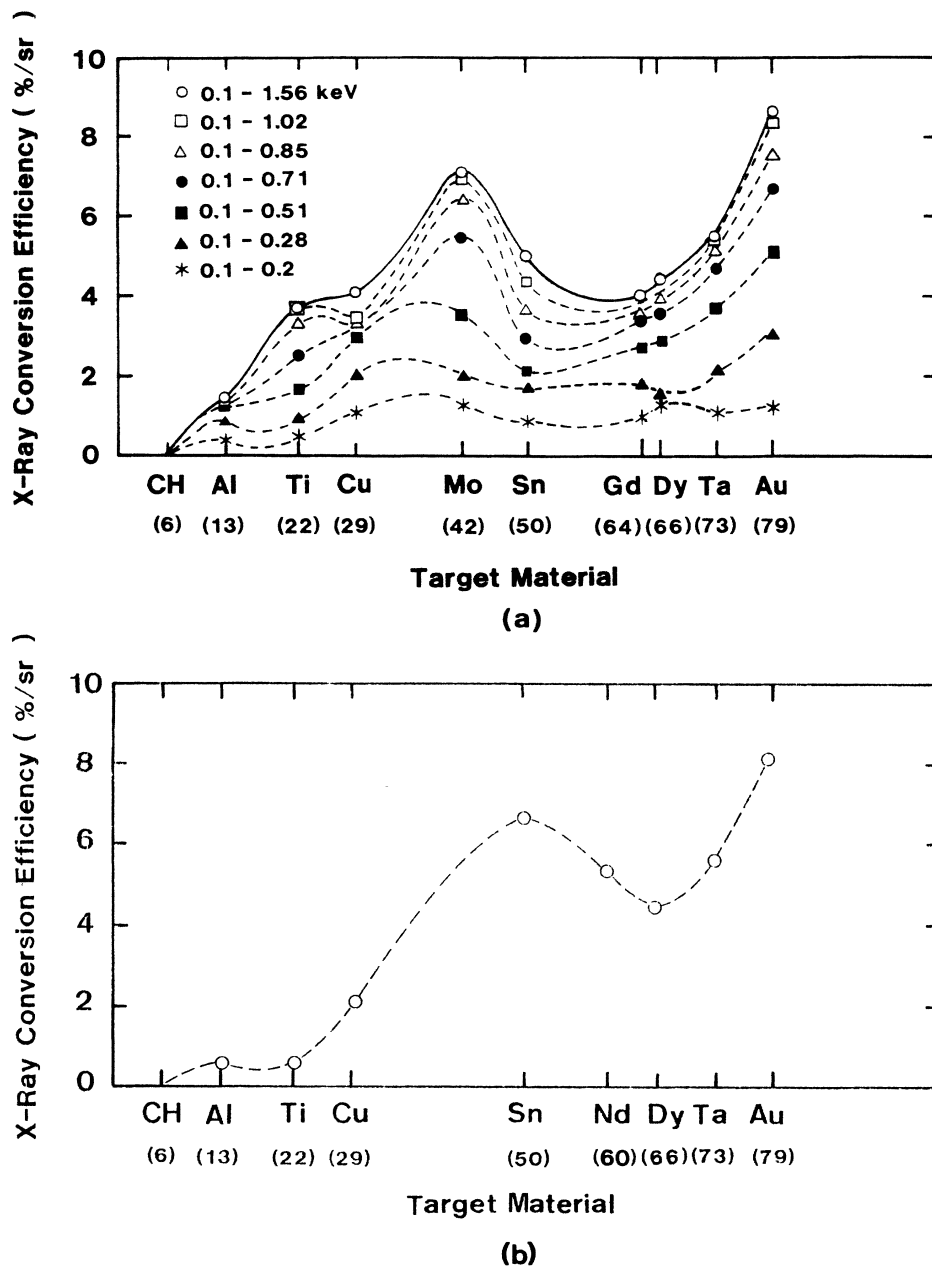


FIG. 13. Atomic-number dependence of x-ray conversion efficiency; (a) experimental results and (b) simulation results.

the humps in the spectrum whose position and intensity depend on the material Z as shown in Fig. 12. The humps originate in electronic transitions in the n th orbital shell of ions as described in Sec. V. We can identify these humps in the spectra sequentially by tracing the change of location of the hump caused by electronic transitions in the same principal quantum number when the Z of the material varies. For example, the hump of titanium at about 0.7 keV in Fig. 12 is identified with L -shell electronic transitions from Grottrian diagrams of transitions in ions.⁴⁵ The humps at about 1.3 keV in the Cu spectrum and at about 0.25 keV in the Al spectrum are found to correspond also to the L -shell electronic transitions by assuming a simple hydrogenic ion model in which the bound energy is proportional to Z^2 . Such estimation is not valid at high- Z materials unless the effective charged

state is used, but it would not be unreasonable to infer that the principal quantum number is responsible for the sequentially appearing hump, given the continuity of the change of its location as a function of the atomic number Z . The inferred principal orbital shells of which electronic transitions are responsible for the hump are denoted in the upper parts of the spectra in Fig. 12. These identifications are also ascertained by the simulation results. In the same manner, the simulation results identify the humps in Fig. 3 as M , N , O , and P shells as denoted in the upper part of the figure.

The simulation results by our hydrodynamic code also predict the undulation structure in fractional efficiency and well reproduced total efficiency change qualitatively, and to some extent quantitatively, as shown by open circles in Fig. 12(b). When we irradiated a CH plate with

higher intensity, $I_L \sim 6 \times 10^{14}$ W/cm², the pulse shape of the XRD signal at the parylene channel had a slightly flat top. This temporal behavior may be evidence of the energy transport inhibition caused by plasma instabilities as suggested by Lee *et al.*⁴⁶ They observed strongly flat-topped shapes in the x-ray pulses from XRD's with low- Z target materials at 1 μ m wavelength and 5×10^{14} W/cm² laser irradiation, and found that the laser intensity threshold for the effect increases with the Z of the target. In our case, the shorter laser wavelength seems to have increased the threshold. Consequently, at the intensity investigated the inhibition does not operate at the higher- Z elements.

There exist dips around Cu ($Z=29$) and Gd ($Z=64$) in x-ray conversion efficiency. This fact seems to be related with the electronic structure of the closed shell which occurs at $Z=28$ and 60 . For Gd, it is expected that the achieved plasma parameters, especially temperature, at dens regions are high enough to ionize the outermost N shell, which contains 32 electrons, up to a fully stripped state, but not so high as to excite the inner M -shell electrons because of the potential gap between N - and M -shell orbits. The same situation may exist for Cu. In these situations, the number of electrons in the outermost shell are so few that the electronic transitions which emit most of the soft x rays decreases. In order to clarify the physical meaning of the above undulation, we try to break down the integrated conversion efficiency into the contributions of the electronic transitions in the respective orbital shells using the spectra shown in Fig. 12. Figure 14 shows the emission intensity by the electrons of respective principal quantum number as a function of the atomic number Z . Figure 14 is considered to be approximate because the estimation of the contribution has some ambiguity in Fig. 12. However, such a diagram suffices to clarify the physical meaning of Z dependence of soft-x-ray emission. It is clearly seen that the shell giving the main contribution moves outward as Z increases. From the main contributing shell, the plausible ion charge state can be inferred and it reflects the plasma temperature at the emission region. Similar behavior was reported by Nagel *et al.*¹ in keV emissions, which were generated in the underdense high-temperature region of 1- μ m laser-produced plasmas. They obtained sharp peaks in Z dependence of the emission. They claimed that peaks occur when K , L , or M binding energies match the electron temperature and concluded that the peak locations change only slightly for wide ranges of laser wavelength, pulse duration, and intensity by coronal model calculations.²⁰ Our results show the maxima at lower Z locations with wide tails. Their heights depend on the principal quantum number.

As clarified in Sec. V, the sub-keV x rays are generated in the plasma region to which we cannot apply the coronal model. The overall spectrum is determined by the summation of photons generated at different locations in the plasma density-temperature profile, hence it is a complicated function of many physical processes. In such a situation it is easily understood that there exist contributions simultaneously from several electronic shells. It means that the peaks should have wide tails and be significantly overlapped with the tail of the next peak as seen for the

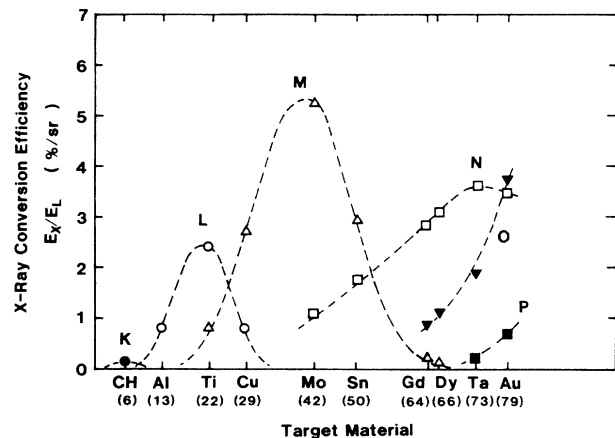


FIG. 14. Atomic-number dependence of x-ray generation from various electronic shells.

elements in Fig. 14. One can expect that these are affected by the plasma density-temperature profile which is set by the energy transport from the laser-energy deposition region. The fact that the locations of the peaks obtained by Nagel *et al.* are higher in Z value than that obtained by us can be qualitatively explained by the difference between their observation range of the photon energy and ours according to Moseley's law $Z \propto (h\nu)^{1/2}$ for electronic transitions to a given principal quantum number.⁴⁷ Unfortunately, the time-of-flight data by the charge collector is too rough to estimate the accurate temperature at the dense plasma region which generates the x ray, so that more detailed correspondence between the ion charge-state distribution and the plasma temperature cannot be obtained in the present experiments. It is only estimated that the molybdenum atom was ionized up to a charge state of Mo^{30+} from the diagram.

VII. SUMMARY AND CONCLUSIONS

Radiant energy spectrum of soft x rays from a 0.53- μ m laser-produced Au plasma has been found to deviate from the simple blackbody radiation spectrum. The spectrum can be fitted by a T_R of about 200 eV for 100–200-eV photons, but the spectral intensity is lower at the $h\nu \geq 500$ eV than the blackbody radiation intensity. The shorter-pulse irradiation produced a clearer dip in the spectrum between 0.3 and 0.6 keV. The conversion efficiency increased as laser-pulse duration.

The hydrodynamic code coupled with a non-LTE average ion model has been used to investigate the dynamics of x-ray generation in laser-produced plasmas and to explain the x-ray spectra at short and long pulses. Simulation clarified the plasma density and temperature regions which are most responsible for x-ray generation in the laser-driven ablation structure of the Au target. The calculated spectra have been found to be in excellent agreement with the experimental results, while the LTE result disagreed with the experimental results. The line spectrum in the LTE model shifts significantly towards a higher-energy side than that in the non-LTE mode. It was concluded from the experimental data of x-ray p - i - n diodes and the simulation study that the hot electrons lit-

tle affect the x-ray emission level and its spectrum profile at laser intensity less than a factor of 10^{14} W/cm². The broadband structures in the spectrum have been inferred to be due to the bound-bound and free-bound transitions of the electrons in the *M*, *N*, *O*, and *P* shells. However, the discrepancy between experimental data and simulation results at $h\nu=100\text{--}300$ eV still remains. It will be improved by incorporating more accurate processes in highly excited states of many electrons by which such low-energy photons can be generated efficiently. The angular distribution of emission is not yet fully understood. A surrounding colder plasma might be also responsible for it.

The spectral dip around 400 eV was found to diminish for a longer pulse. This tendency could not be satisfactorily reproduced by the simulation, although this dip is due to the minimum of the emission level between the bound-bound emissions in the *O* shell and the *N* shell.

Soft-x-ray emission reflects the transport of absorbed laser energy into the target plasma. It may become a good diagnostic tool to investigate the energy transport into the high-density plasma region. The experimental results showed the lateral energy transport was not predominant. It is conclusively found that the emission level is sensitive to the axial energy transport inhibition factor f which

operates especially for steep density gradient at a shorter pulse. The best fitted value of f has been found to be 0.03.

Z dependence of the spectra in the soft-x-ray region (0.1–1.6 keV) has been experimentally obtained for the first time. The x-ray conversion efficiency was found to increase gradually with some undulation as Z increases. There exist dips around Cu ($Z=29$) and Gd ($Z=64$) in x-ray conversion efficiency. These minima in the efficiency have been concluded to be due to the electronic structure of the closed shell which occurs at $Z=28$ and 60. The simulation results explained well qualitatively and to some extent quantitatively the undulation obtained experimentally.

These results will give physical insight in x-ray generation dynamics in laser-produced plasmas and will provide useful information for producing stimulated emissions in xuv region and x-ray sources for microlithography as well as for inertial-confinement fusion.

ACKNOWLEDGMENTS

We are grateful to the GEKKO-IV laser group for laser operation and also to Dr. K. Nishihara for helpful discussion, and to Dr. T. Boehly for many valuable comments.

-
- ¹D. J. Nagel, P. G. Burkhalter, G. A. Doscheck, C. M. Dozier, U. Feldman, B. M. Klein, and R. R. Whitlock, Naval Reserach Laboratory Report No. 7838, 1974 (unpublished).
- ²K. Eidmann, M. H. Key, and R. Siegel, *J. Appl. Phys.* **47**, 2402 (1976).
- ³H. Pépin, B. Grek, F. Rheault, and D. J. Nagel, *J. Appl. Phys.* **48**, 3312 (1977).
- ⁴D. J. Nagel, P. G. Burkhalter, C. M. Dozier, J. F. Holzrichter, B. M. Klein, J. M. McMahon, J. A. Stamper, and R. R. Whitlock, *Phys. Rev. Lett.* **33**, 743 (1974).
- ⁵P. Burkhalter, U. Feldman, and R. Cowan, *J. Opt. Soc. Am.* **64**, 1058 (1974).
- ⁶L. Chase, W. Jordan, J. Perez, and R. Johnston, *Phys. Rev. A* **13**, 1497 (1976).
- ⁷D. Colombant and G. F. Tonon, *J. Appl. Phys.* **44**, 3524 (1973).
- ⁸R. K. Landshoff and J. D. Perez, *Phys. Rev. A* **13**, 1619 (1976).
- ⁹D. Duston and J. Davis, *Phys. Rev. A* **21**, 1664 (1980), and references therein.
- ¹⁰J. Mizui, N. Yamaguchi, T. Yamanaka, and C. Yamanaka, *Phys. Rev. Lett.* **39**, 619 (1977).
- ¹¹H. D. Shay, R. A. Haas, W. L. Kruer, M. J. Boyle, D. W. Phillion, V. C. Rupert, H. N. Kornblum, F. Rainer, V. W. Slivinsky, L. N. Koppel, L. Richards, and K. G. Tirsell, *Phys. Fluids* **21**, 1634 (1978).
- ¹²J. Mizui, M. Yamaguchi, S. Takagi, and K. Nishihara, *Phys. Rev. Lett.* **47**, 1000 (1981).
- ¹³J. L. Bocher, M. Decroisette, P. A. Holstein, M. Louis-Jacquet, B. Meyer, A. Saleres, and G. Thiell, *Phys. Rev. Lett.* **52**, 823 (1984).
- ¹⁴F. Amiranoff, R. Fabbro, E. Fabre, C. Garban, J. Virmont, and M. Weinfeld, *Phys. Rev. Lett.* **43**, 522 (1979).
- ¹⁵B. Yaakobi, T. Boehly, P. Bourke, Y. Conturie, R. S. Craxton, J. Delettrez, J. M. Forsyth, R. D. Frankel, L. M. Goldman, R. L. McCrory, M. C. Richardson, W. Seka, D. Shvarts, and J. M. Soures, *Opt. Commun.* **39**, 175 (1981).
- ¹⁶W. C. Mead, E. M. Campbell, K. G. Estabrook, R. E. Turner, W. L. Kruer, P. H. Y. Lee, B. Pruett, V. C. Rupert, K. G. Tirsell, G. L. Stradling, F. Ze, C. E. Max, and H. D. Rosen, *Phys. Rev. Lett.* **47**, 1289 (1981).
- ¹⁷P. D. Rockett, W. C. Priedhosky, D. V. Giovanielli, *Phys. Fluids* **25**, 1286 (1982).
- ¹⁸H. Nishimura, F. Matsuoka, M. Yagi, K. Yamada, S. Nakai, G. H. McCall, and C. Yamanaka, *Phys. Fluids* **26**, 1688 (1983).
- ¹⁹W. C. Mead, E. M. Campbell, K. G. Estabrook, R. E. Turner, W. L. Kruer, P. H. Y. Lee, B. Pruett, V. C. Rapert, K. G. Tirsell, G. L. Stradling, F. Ze, C. E. Max, M. D. Rosen, and B. F. Lasinski, *Phys. Fluids* **26**, 2316 (1983). They provided the x-ray spectrum from a gold target in the photon energy range from 250 eV to 1.1 keV at a laser intensity of 3×10^{14} W/cm² in 600 psec with the incidence angle of 30° in *P* polarization. The observation angle was 60°.
- ²⁰K. M. Glibert, J. P. Anthes, M. A. Gusinow, M. A. Plamer, R. R. Whitlock, and D. J. Nagel, *J. Appl. Phys.* **51**, 1449 (1980).
- ²¹T. Mochizuki, S. Sakabe, K. Okada, H. Shiraga, T. Yabe, and C. Yamanaka, *Jpn. J. Appl. Phys.* **22**, L133 (1983).
- ²²J. Oxenius, *Astron. Astrophys.* **76**, 312 (1979), and references therein.
- ²³D. Duston, R. W. Clark, J. Davis, and J. P. Apruzese, *Phys. Rev. A* **27**, 1441 (1983).
- ²⁴K. Okada, T. Mochizuki, M. Hamada, M. Ikeda, H. Shiraga, T. Yabe, and C. Yamanaka, *Jpn. J. Appl. Phys.* **22**, L671 (1983).
- ²⁵R. H. Day, P. Lee, E. B. Saloman, and D. J. Nagel, *J. Appl. Phys.* **52**, 6965 (1981).
- ²⁶B. L. Henke, P. Lee, T. J. Tanaka, R. L. Shimabukuro, and B.

- K. Fujikawa, *At. Data Nucl. Data Tables* **27**, 1 (1982).
- ²⁷The effects of long-term cathode aging through exposure to air was also studied in Ref. 25. After extensive handling over a range of six months, a change of 50% in quantum efficiency was found. We replaced the cathode typically every two months or just before we conducted a series of target shots.
- ²⁸E. M. Campbell, F. Ze, D. W. Philion, and V. C. Rupert, Lawrence Livermore National Laboratory Report No. UCRL-50021-79, 1979 (unpublished).
- ²⁹N. M. Ceglio, R. L. Kauffman, A. M. Hawryluk, and H. Medeck, *Appl. Opt.* **22**, 318 (1983). They obtained the time-resolved spectrum in arbitrary scale at the same experimental conditions as that used by Mean *et al.* (Ref. 19) except for the laser-pulse duration; they used 700-psec pulses. Since their spectrum shapes appear to be very similar in laser-pulse duration, we adopt the spectrum at the laser intensity peak and scale it to coincide with the value by Mean *et al.* at $h\nu=250$ eV.
- ³⁰Y. B. Zel'dovich and Y. P. Raizer, *Physics of Shockwaves and High Temperature Hydrodynamic Phenomena* (Academic, New York, 1966), p. 277.
- ³¹When the laser absorption rate is dominated by a classical absorption process, it slowly increases with the plasma scale length at the conditions under which stimulated back reflections are not set. See, for example, S. Sakabe, T. Mochizuki, and C. Yamanaka, *Jpn. J. Appl. Phys.* **23**, 460 (1984).
- ³²T. Yabe, K. Mima, K. Yoshikawa, H. Takabe, and M. Hamano, *Nucl. Fusion* **21**, 803 (1981).
- ³³S. Kiyokawa, T. Yabe, and T. Mochizuki, *Jpn. J. Appl. Phys.* **22**, L772 (1983).
- ³⁴D. E. Post, R. V. Jensen, C. B. Tarter, W. H. Grasberger, and W. A. Lokke, *At. Data Nucl. Data Tables* **20**, 397 (1977).
- ³⁵R. M. More, Lawrence Livermore Laboratory Report No. UCRL-84991, 1981 (unpublished).
- ³⁶H. Mayer, Los Alamos Scientific Laboratory Report No. LA-647, 1947 (unpublished).
- ³⁷W. A. Lokke and W. H. Grasberger, Lawrence Livermore Laboratory Report No. UCRL-52276, 1977 (unpublished).
- ³⁸S. Kiyokawa and T. Yabe (unpublished).
- ³⁹The spherical one-dimensional treatment of this kind was also used in Ref. 19, where a radius of curvature is taken to be twice the laser-spot diameter. This treatment may be adequate for a long laser pulse. For a short pulse discussed in this paper, it may be reasonable to use the laser-spot radius as the radius of curvature.
- ⁴⁰W. C. Mead, E. M. Campbell, W. L. Kruer, R. E. Turner, C. W. Hatcher, D. S. Bailey, P. H. Y. Lee, J. Foster, K. G. Tirsell, B. Pruett, N. C. Holmes, J. T. Trainer, G. L. Stradling, B. F. Lasinski, C. E. Max, and F. Ze, *Phys. Fluids* **27**, 1301 (1984).
- ⁴¹M. Rosen, D. Phillion, V. Rupert, W. Mead, W. Kruer, J. Thomson, H. Kornblum, V. Slivinsky, G. Caporaso, M. Boyle, and K. Tirsell, *Phys. Fluids* **22**, 2020 (1979).
- ⁴²W. B. Fechner, C. L. Shepard, Gar. E. Busch, R. J. Schroeder, and J. A. Tarvin, *Phys. Fluids* **27**, 1552 (1984), and references therein.
- ⁴³K. Estabrook and W. L. Kruer, *Phys. Rev. Lett.* **40**, 42 (1978).
- ⁴⁴The self-induced magnetic field has been recognized as a candidate for flux inhibition. As shown in the paper by A. Nishiguchi *et al.*, *Phys. Rev. Lett.* **53**, 262 (1984), the magnetic field is convected and amplified towards the ablation front from the critical point maintaining $\omega_{ce}\tau_{ei}=\text{const}$. The flux inhibition by this magnetic field occurs throughout the ablation region without localizing near the critical point in contrast to that by other mechanisms.
- ⁴⁵S. Bashkin and J. O. Stoner, Jr., *Atomic Energy-Level and Grotrian Diagrams* (North-Holland, Amsterdam, 1978), Vol. II.
- ⁴⁶G. McClellan, P. H. Y. Lee, and G. Caporaso, *Phys. Rev. Lett.* **44**, 658 (1980).
- ⁴⁷See, for example, B. K. Agarwal, *X-Ray Spectroscopy* (Springer, Berlin, 1979), Chap. 2.

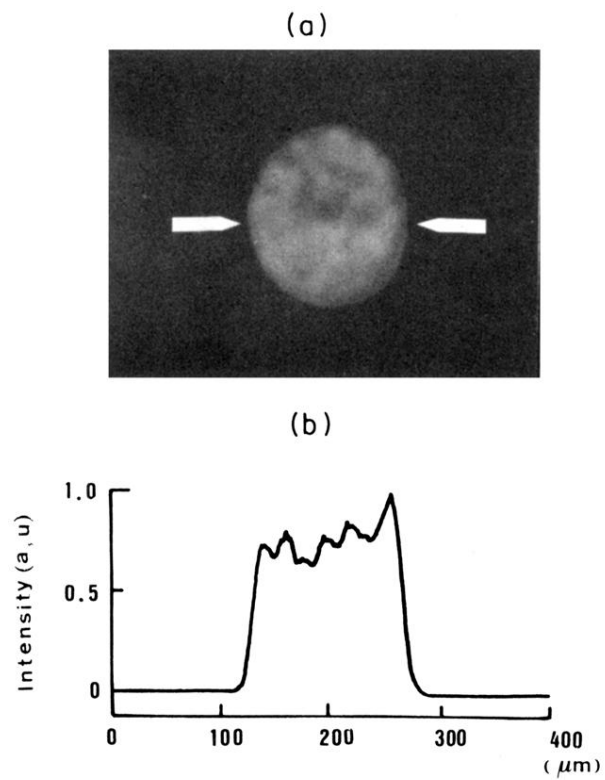


FIG. 1. (a) A typical intensity image of the $0.53\text{-}\mu\text{m}$ laser pulse in the target plane. The average intensity is 10^{14} W/cm^2 . (b) A profile of the laser intensity in the target plane.

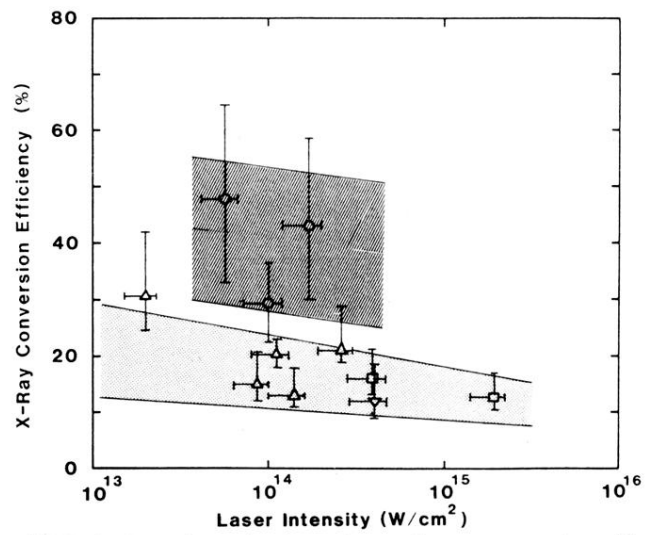


FIG. 6. Laser-intensity dependence of x-ray conversion efficiency for various laser-pulse durations: \circ , 1.0 nsec; \triangle , 0.23–0.25 nsec; \square , 0.15, nsec; ∇ , 0.1 nsec.